Publishing Excellence
Inspiring Progress

ISSN: 0000-0000 www.aristonpubs.com/journal/science-of-optics-and-photonics https://doi.org/10.69626/sop.2026.0006

RESEARCH ARTICLE

Visible-Near-Infrared (350 - 1050 THz) Silver Bowtie Nanoantenna for Optical Rectenna Energy Harvesting : Dependent Full - Wave Study

Saurav Mishra, Brijesh Kumar Pandey Singh*, Pradutt Kumar Bharti

ABSTRACT: Optical rectennas-nanoantennas coupled to ultrafast rectifiers-offer a bandgap-free route to converting solar radiation into direct-current (DC) power, but their realisation requires antennas that combine broadband impedance matching with strong field confinement at the rectifier location. In this work, a silver bowtie nanoantenna (arm length 150 nm, flare angle 90°) on a 10 nm SiO_2 layer is designed and analysed by full-wave finite-element simulation (COMSOL Multiphysics 6.2, RF Module) across the visible-near-infrared band (350-1050 THz; free-space wavelength 857-286 nm). Two feed-gap widths (20 and 30 nm) are compared in terms of reflection coefficient, input impedance, near-field distribution, radiation pattern and realised gain. Both designs resonate at ≈650 THz (≈461 nm) with a minimum S_{11} of −24.2 dB (20 nm) and −24.6 dB (30 nm). The −10 dB impedance bandwidth extends from ≈480 to ≈875 THz (≈390 THz, ≈57% fractional bandwidth). The maximum realised gain rises from ≈0.2 dBi at 350 THz to 3.25-3.28 dBi at 750 THz, and a dipole-like radiation pattern is maintained up to ≈850 THz, above which higher-order modes distort the pattern. Below 850 THz, changing the gap from 20 to 30 nm alters the minimum S_{11} by less than 0.5 dB and the gain by less than 0.05 dB, indicating tolerance to the gap variations typical of electron-beam lithography, whereas the peak gap field increases by ≈50% for the narrower gap. The strongest near fields occur at the feed gap, identifying it as the natural site for a metal-insulator-metal tunnelling diode. The remaining obstacles to a complete rectenna-rectifier cut-off frequency, antenna-diode impedance matching, polarisation and the partial coherence of sunlight-are discussed.

Keywords: Optical Rectenna; Bowtie Nanoantenna; Plasmonics; Solar Energy Harvesting; Finite-Element Method; Impedance Matching.

Received: 05 March 2026; Revised: 14 April 2026; Accepted: 5 May 2026; Published Online: 21 May 2026

1. INTRODUCTION

The growing global demand for clean electricity has made photovoltaics (PV) the fastest-growing renewable generation technology [1, 2]. The efficiency of a single-junction PV cell is, however, bounded by the detailed-balance limit of ≈33%, because photons with energies below the bandgap are not absorbed and the excess energy of above-gap photons is lost as heat [3]. Record crystalline-silicon cells have reached ≈26.7% [4], and wafer-based modules are rigid and comparatively bulky, which complicates their integration into miniaturized, autonomous micro systems and sensor nodes [5].

An alternative conversion route, first proposed by Bailey [6], treats sunlight as an electromagnetic wave rather than as a stream of photons. In such a rectenna, an antenna converts the incident field into an alternating current at the optical frequency, which is then rectified by an ultrafast diode. Because the conversion is not mediated by a semiconductor bandgap, the spectral response is set by the antenna geometry, and theoretical analyses have predicted

Nanofluid Laboratory, Department of Physics and Material Science, Madan Mohan Malaviya University of Technology, Gorakhpur 273010, Uttar Pradesh, India

*Author to whom correspondence should be addressed: bkpmmmec11@gmail.com (B. Pandey)

© Ariston Publications 2026. All rights reserved.

Table 1. Comparison of crystalline-silicon photovoltaics and optical nanoantenna rectennas.

Feature	Optical Nanoantenna Rectenna	Crystalline-Si Photovoltaics
Conversion mechanism	Antenna coupling of the optical field followed by ultrafast rectification [6, 7]	Photovoltaic effect in a p–n junction [3]
Spectral response	Set by antenna geometry; broadband per element	Photons above the 1.12 eV bandgap
Fundamental loss channels	Diode cut-off, antenna–diode mismatch, partial coherence [8, 9]	Sub - band-gap transmission, thermalization [3]
Demonstrated efficiency	Far below 1% at visible frequencies [10]	≈ 26.7% record cell [4]
Form factor	Nanoscale, lithographically defined; compatible with flexible substrates [11]	Wafer-based, rigid modules
Technology maturity	Laboratory research	Commercial

high conversion efficiencies, particularly for narrow-band or highly coherent radiation [7, 12]. For broadband, partially coherent sunlight the achievable efficiency is lower and depends strongly on the antenna bandwidth, polarisation, and the rectifier characteristics [8, 13]. Table 1 summarises the main differences between the two conversion routes. Scaling antenna concepts from radio to optical frequencies requires accounting for the plasmonic, dispersive response of metals, which shortens the effective resonant length and introduces ohmic loss [14–17]. Nanoantenna-based rectennas have been demonstrated experimentally in the mid-infrared, for example bowtie and related nanoantennas coupled to metal–insulator–metal (MIM) diodes at 28.3 THz [18, 19] and nanoantenna-coupled metal–oxide–semiconductor tunnel diodes [20], while rectification of visible light has been shown with carbon-nanotube antenna arrays [10]. Large-area nanoantenna arrays have also been fabricated on flexible substrates [11]. In all cases the measured efficiencies remain low, mainly because of the limited cut-off frequency of available diodes and the large impedance mismatch between antenna and diode [9, 21, 22]. Improving the antenna—its bandwidth, matching and field confinement at the diode site—is therefore one of the two key levers, the other being the rectifier. A note on terminology is warranted. The term “terahertz band” conventionally refers to 0.1– 10 THz [23, 24]. In this work, terahertz (THz) is used only as the unit of frequency for the visible–near-infrared band of 350–1050 THz (857–286 nm), which contains a large fraction of the solar irradiance. The antenna studied here therefore targets solar radiation; it does not address harvesting of terrestrial thermal emission, which peaks in the mid-infrared near 30 THz and requires antennas roughly 20 times larger [25]. The bowtie geometry is a natural candidate for broadband operation: its triangular arms approximate a biconical antenna, whose input impedance varies slowly with frequency [26, 27]. At optical frequencies, metallic bowties additionally concentrate the field in the feed gap, with a resonance and field enhancement that depend on the gap width [28–31]. The concepts of input impedance and impedance matching carry over to optical nanoantennas when the gap is treated as a nanocircuit load [32, 33]. These properties make the bowtie attractive as the receiving element of an optical rectenna for self-powered microsystems and nanosensor networks [5, 34]. The contributions of this work are as follows: (i) a silver bowtie nanoantenna on SiO_2 is designed for the 350–1050 THz band and characterised by full-wave finite-element simulation; (ii) the effect of feed-gap width (20 and 30 nm) on the reflection coefficient, input impedance, near-field distribution, radiation pattern and realised gain is quantified; (iii) the tolerance of the design to gap variations is assessed; and (iv) the steps required to turn the antenna into a working rectenna are identified. Section 2 describes the design and numerical method, Section 3 presents and discusses the results, and Section 4 concludes the paper.

2. ANTENNA DESIGN AND SIMULATION METHODOLOGY

2.1 Antenna geometry

The antenna consists of two identical, coplanar triangular silver arms placed tip-to-tip and separated by a feed gap g (Fig. 2). Each arm has a height h0 = 150 nm and a flare angle of 90°. The arms rest on a 10 nm SiO_2 layer that extends 60 nm beyond the antenna on each side. Two gap widths, g = 20 and 30 nm, were studied; all other dimensions were kept constant. The geometrical parameters are listed in Table 2.

2.2 Materials

Silver was chosen for the arms because it has the lowest optical loss among the noble metals across most of the visible range [35, 36].

© Ariston Publications 2026. All rights reserved.

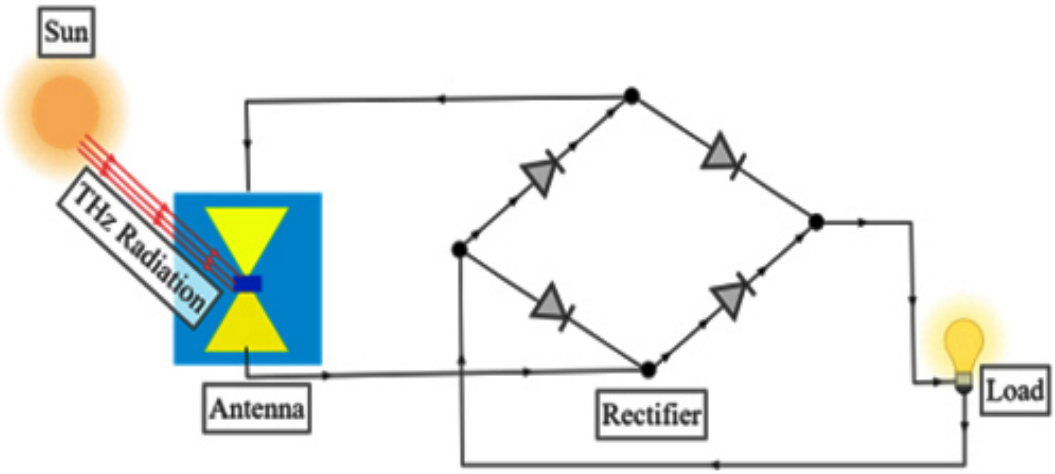


Fig. 1. Conceptual schematic of an optical rectenna: the nanoantenna couples incident solar radiation to an AC current at the optical frequency, which is rectified and delivered to a load. The diode bridge is shown for illustration only; at visible frequencies a single ultrafast MIM tunnelling diode placed in the feed gap is the practical choice [9].

It was modelled as a dispersive metal with a frequency dependent complex permittivity, so that its plasmonic response and ohmic loss in the visible–near-infrared range are included [36]. The SiO_2 layer was modelled as a non-dispersive dielectric with refractive index ≈1.45 [37] and a loss tangent of 1×10^{-4}, consistent with its negligible absorption in the visible and near-infrared.

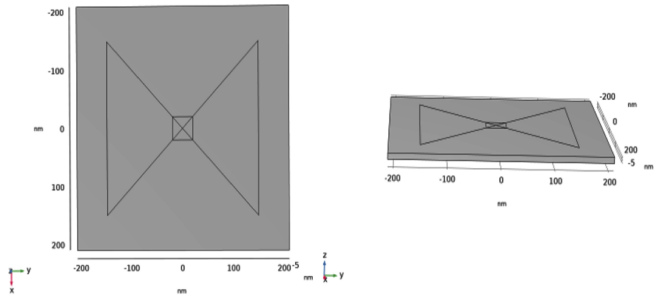


Fig. 2. Geometry of the bowtie nanoantenna on the SiO_2 layer: top view (left) and perspective view (right). Dimensions in nm.

Table 2. Geometrical and simulation parameters of the bowtie nanoantenna.

Parameter	Symbol	Value
Arm height (feed to base)	h_0	150 nm
Flare angle	θ	90°
Feed-gap width	g	20, 30 nm
SiO_2 layer thickness	t_s	10 nm
Substrate padding around antenna	–	60 nm
Frequency range (step)	f	350–1050 THz (50 THz)
Free-space wavelength	$\lambda_0 = c/f$	857–286 nm

2.3 Simulation setup

Full-wave simulations were performed with the Electromagnetic Waves, Frequency Domain interface of the RF Module in COMSOL Multiphysics 6.2, which solves Maxwell's equations in the frequency domain with the finite-element method [38].

2.3.1 Computational domain and boundary conditions

The antenna was placed at the centre of a spherical air domain of radius ≈600 nm (Fig. 3), surrounded by a perfectly matched layer (PML) [39] of thickness 0.15λ0.

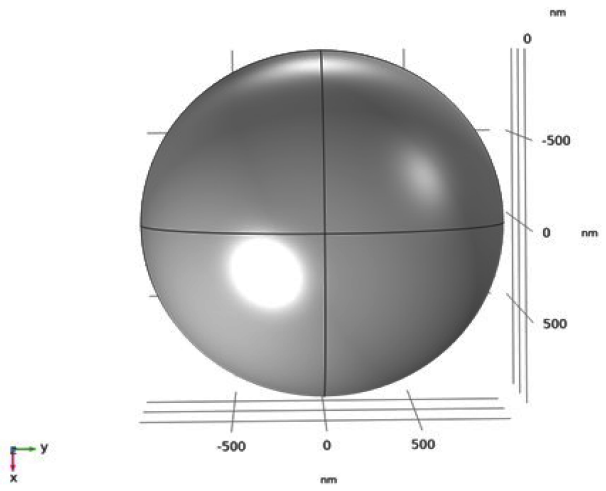


Fig. 3. Spherical computational domain enclosing the antenna and terminated by a perfectly matched layer.

A scattering boundary condition was applied on the outer surface of the PML to suppress any residual reflection. Farfield quantities were obtained from a near-to-far-field transformation evaluated on the inner boundary of the PML.

© Ariston Publications 2026. All rights reserved.

Table 3. Summary of the simulated performance for the two gap widths.

Gap g (nm)	Resonance (THz)	$S_{11,\min}$ (dB)	-10 dB band (THz)	FBW (%)	Gain at 650 THz (dBi)	Peak gain @ freq. (dBi)
20	650	-24.2	≈ 480-865	≈ 57	2.31	3.25 @ 750 THz
30	650	-24.6	≈ 485-875	≈ 57	2.31	3.28 @ 750 THz

2.3.2 Excitation

The antenna was excited by a lumped port spanning the feed gap, with reference impedance Zref. By reciprocity, the transmitting-mode gain obtained in this way equals the receiving-mode gain, and the effective aperture of the antenna is Ae = λ02G/4π [27]. Because the near-field maps in Section 3.1 are computed under port excitation, they show the spatial distribution of the field rather than the enhancement relative to an incident plane wave.

2.3.3 Mesh

A free tetrahedral mesh was used, with a maximum element size of λmin/10 (≈29 nm at 1050 THz) in the air domain and local refinement in the metal and the feed gap to resolve the strongly localised fields; the PML was meshed with swept elements (Fig. 4).

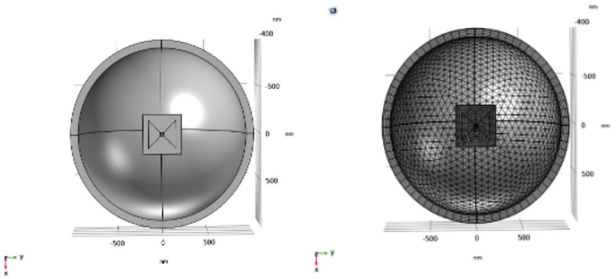


Fig. 4. Cross-section of the computational domain (left) and the corresponding tetrahedral mesh with local refinement around the antenna (right).

2.3.4 Solver and extracted quantities

The resulting linear systems were solved with the MUMPS direct solver [40] on a highperformance computing system for 15 frequencies between 350 and 1050 THz in 50 THz steps. The reflection coefficient at the port is

$$\Gamma = \frac{Z_{\text{in}} - Z_{\text{ref}}}{Z_{\text{in}} + Z_{\text{ref}}}, S_{11}(\text{dB}) = 20\log_{10}|\Gamma| \quad (1)$$

where $Z_{\text{in}} = R_{\text{in}} + jX_{\text{in}}$ is the input impedance of the antenna, with R_{in} accounting for radiation and ohmic loss and X_{in} for the stored reactive energy [41]. An S_{11} of -10 dB corresponds to 10% of the incident power being reflected; this threshold defines the impedance bandwidth $[f_L, f_H]$ and the fractional bandwidth FBW $= \frac{2(f_H - f_L)}{f_H + f_L}$. The realised gain, which includes mismatch and ohmic losses, is

$$G_r(\theta,\varphi) = \left(1 - |\Gamma|^2\right) e_{\text{rad}} D(\theta,\varphi) \quad (2)$$

where e_{rad} is the radiation efficiency and D the directivity [27]. The near-field distribution, the input-impedance locus on the Smith chart, and the two- and three-dimensional far-field patterns were also extracted.

3. RESULTS AND DISCUSSION

3.1 Near-field distribution

Figure 5 shows the electric-field norm in the plane of the antenna for the 30 nm gap at all 15 simulated frequencies; the corresponding maps for the 20 nm gap are given in Supplementary Fig. S1. For both gaps, the field is concentrated in the feed gap and along the edges and outer vertices of the triangular arms, as expected for a bowtie antenna [28, 30]. The gap field is strongest between ≈450 and ≈850 THz, i.e. around the impedance resonance discussed in Section 3.2. Above ≈900 THz, a growing fraction of the field shifts towards the outer corners of the arms, consistent with the excitation of higher-order modes; the same frequencies show distorted radiation patterns (Section 3.4).

Figure 6 compares the field distributions at 650 THz, where the reflection coefficient is minimum, for the two gaps. The maximum field occurs inside the gap, with secondary maxima at the outer vertices. Under the same port excitation, the peak field increases from ≈5.3 × 10^7 V/m for the 30 nm gap to ≈8.0 × 10^7 V/m for the 20 nm gap, i.e. by ≈50%, consistent with the gap-dependent field enhancement reported for optical bowties [28, 30]. The narrower gap therefore offers the strongest drive for a rectifier, at no measurable cost in impedance matching (Section 3.2). Localising the

© Ariston Publications 2026. All rights reserved.

field within the 20–30 nm gap is advantageous for rectification, because a tunnelling diode placed in the gap experiences the largest voltage while its small area keeps its capacitance low [9].

3.2 Reflection coefficient

Figure 7 shows S_{11} versus frequency for the two gap widths, and the key metrics are summarised in Table 3. Both designs show a single, well-defined resonance at 650 THz (461 nm), with minimum S_{11} values of −24.6 dB (30 nm) and −24.2 dB (20 nm). At −24.6 dB only ≈0.35% of the incident power is reflected at the port.

The −10 dB band extends from ≈480 to ≈875 THz, corresponding to a fractional bandwidth of ≈57%, and the band edges differ by less than ≈10 THz between gaps, which is within the resolution of the 50 THz frequency sweep. Below the band, the match degrades steadily to ≈−4.5 dB at 350 THz, whereas above it S_{11} remains close to −9 to −10 dB up to 1050 THz. A narrower gap increases the capacitive coupling between the arms and is generally expected to red-shift the bowtie resonance [28, 30]. No shift is resolved here, which indicates that for this geometry the resonance is governed mainly by the arm length; a finer frequency sweep (≤10 THz) would be required to quantify small shifts. The weak dependence of both the resonance and the matching on the gap width is a practical advantage, because gap widths realised by electron-beam lithography typically deviate from their nominal values by several nanometres.

3.3 Input impedance

Figure 8 shows the S_{11} locus on the Smith chart, normalised to Zref, with frequency indicated by colour. For both gaps the locus forms a loop that passes closest to the chart centre near 650 THz, where Zin is close to Zref and the residual reactance is small. Below the resonance the locus lies in the upper half of the chart (inductive reactance), and above it the locus moves into the lower half (capacitive reactance) before turning back towards the left side of the chart at the highest frequencies. The two loci nearly coincide, confirming that the gap width has only a minor effect on the input impedance in this range. The residual reactance away from resonance could be reduced by adjusting the arm length or flare angle, or by adding a reactive load in the gap [32, 33].

It should be emphasised that the matching reported here is relative to the port reference impedance. In a rectenna the relevant load is the diode, whose resistance and capacitance at optical frequencies differ substantially from typical port impedances [11,21]. The present results therefore characterise the antenna itself; co-design of the antenna and diode impedance is addressed in Section 3.7.

3.4 Radiation patterns

3.4.1 Two-dimensional patterns

Figure 9 shows the normalised far-field patterns in a principal plane of the antenna for all frequencies. For each gap the pattern has two broad main lobes separated by nulls at 90° and 270°, i.e. a dipole-like figure-of-eight pattern. Between 350 and ≈900 THz the patterns for different frequencies are similar, with a shallow dip near 0° and 180° within each lobe. At 950–1000 THz the lobes become distorted, and at 1050 THz the pattern changes to single lobes centred at 0° and 180°, consistent with the onset of higher-order modes noted in Section 3.1. The patterns for the two gaps are nearly identical. A single bowtie is therefore bidirectional rather than omnidirectional: it receives efficiently over a wide range of angles around the lobe maxima but not along the null directions. It is also linearly polarised along the bowtie axis. Both points are relevant for harvesting unpolarised, diffuse light and are discussed in Section 3.7.

3.4.2 Three-dimensional patterns

Figure 10 shows the three-dimensional realised-gain patterns for the 30 nm gap (patterns for the 20 nm gap are given in Supplementary Fig. S2). Up to ≈850 THz the pattern is a slightly flattened torus with a null along the bowtie axis, as expected for a dipole-like antenna [27], and the colour-scale maxima give the maximum realised gain at each frequency (Fig. 12). From 900 to 1000 THz the pattern becomes irregular, and at 1050 THz the null rotates into a different plane, consistent with the 2D patterns in Fig. 9. Figure 11 compares the patterns of the two gaps at 650 THz.

3.5 Realised gain

The maximum realised gain at each frequency is plotted in Fig. 12. For both gaps, the gain increases from ≈0.2 dBi at 350 THz, where the antenna is electrically small and poorly matched, to 2.1–2.4 dBi between 500 and 650 THz. These values are close to the 2.15 dBi directivity of a half-wave dipole [27], consistent with the dipole-like patterns in Figs. 9 and 10. The gain then rises to 3.23–3.24 dBi at 700

© Ariston Publications 2026. All rights reserved.

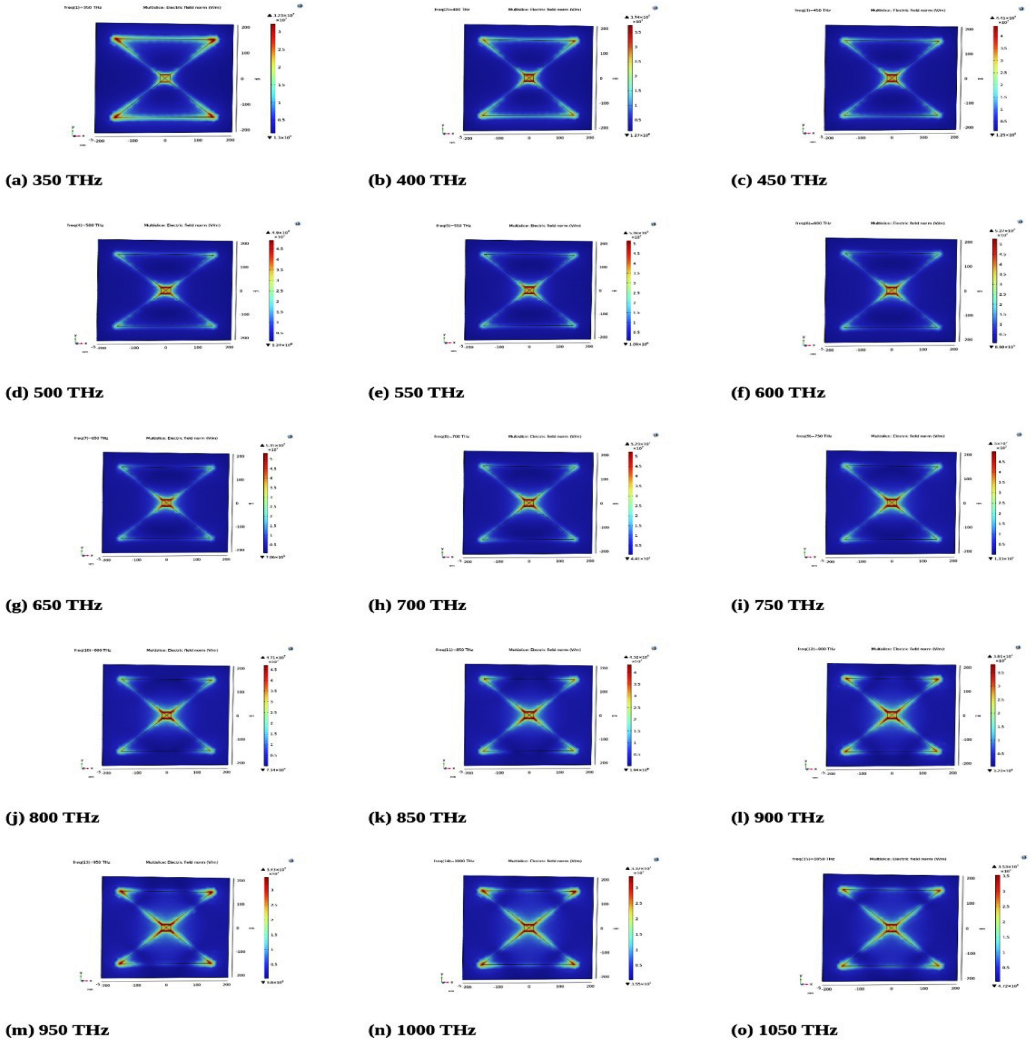


Fig. 5. Electric-field norm (V/m) in the antenna plane for g = 30 nm at frequencies from (a) 350 THz to (o) 1050 THz.

THz and reaches its maximum of 3.25 dBi (20 nm) and 3.28 dBi (30 nm) at 750 THz, before decreasing slightly to 2.95–3.06 dBi at 850 THz. Above 850 THz the gain becomes non-monotonic, with minima at 900 THz (as low as 2.39 dBi for the 20 nm gap) and at 1000 THz (2.06 dBi) and a recovery to 3.11–3.18 dBi at 1050 THz. These variations coincide with the pattern changes discussed in Section 3.4 and are attributed to higher-order modes; with a 50 THz sweep step, narrower features may not be fully resolved. Below 850 THz, the gain differs by less than 0.05 dB between the two gaps, whereas above 850 THz the difference reaches ≈0.3 dB at 950 THz. Within the −10 dB band (≈480– 875 THz) the gain stays between 2.1 and 3.3 dBi. At 650 THz, a gain of 2.31 dBi corresponds to an effective aperture of Ae ≈ 0.029 μm² (≈2.9 × 10^4 nm²), which sets the power intercepted by a single element.

3.6 Comparison with previous work

Previous nanoantenna rectenna studies have mostly targeted the infrared: nanoantenna arrays have been fabricated on flexible substrates [11], bowtie and related nanoantennas have been combined with MIM diodes at 28.3 THz [18, 19], and nanoantenna-coupled MOS tunnel diodes have rectified long-wave infrared radiation [20]. At visible–near-infrared frequencies, rectification has been demonstrated with carbon-nanotube antenna–diode arrays [10], and theoretical upper bounds on nanoantenna harvesting efficiency have been derived for the solar spectrum [8]. A direct comparison of gain and S_{11} values across studies is of limited meaning, because the reported quantities depend on the port reference impedance, the substrate, the metal model and whether gain or realised gain is reported. The main distinguishing

 © Ariston Publications 2026. All rights reserved.

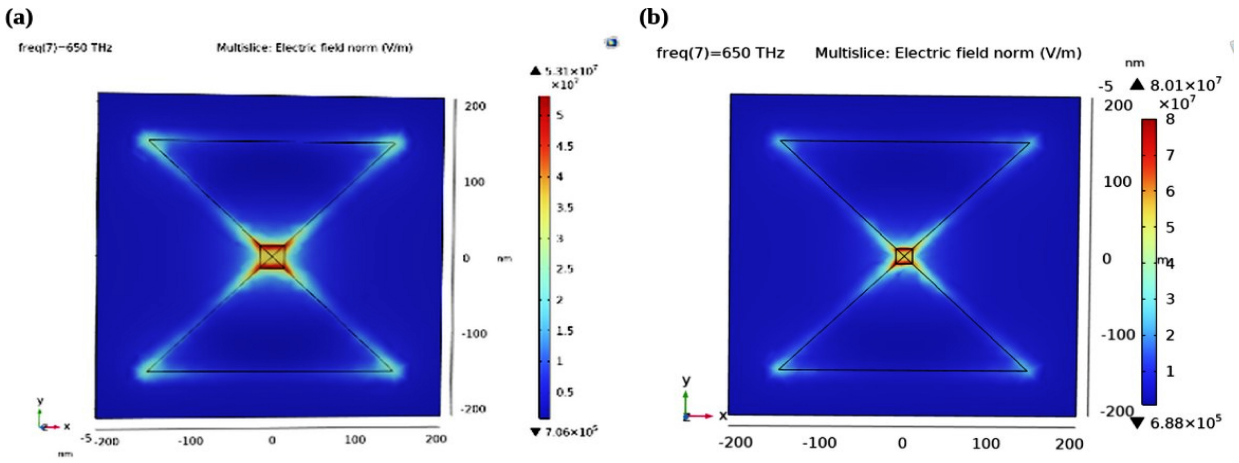


Fig. 6. Electric-field norm (V/m) in the antenna plane at 650 THz for (a) g = 30 nm and (b) g = 20 nm.

features of the present design are its operation in the visible–near-infrared band, where most experimental rectennas have not yet operated efficiently, and its broad −10 dB impedance bandwidth of ≈57%, which is insensitive to the gap width between 20 and 30 nm. Unlike the experimental studies cited above, however, the present work is limited to the antenna and does not include a rectifier.

3.7 Limitations and route towards a complete rectenna

Several issues must be resolved before the antenna can be used in a working rectenna. First, the rectifier must respond at optical frequencies: for a diode with resistance RD and capacitance CD, the cut-off condition $1/(2\pi RDCD) > 650$ THz requires $RDCD < 0.25$ fs, which is difficult to achieve with MIM diodes because reducing the capacitance by shrinking the junction area increases the resistance [9, 21]. Placing a tunnelling junction with an area of a few hundred nm² in the 20–30 nm gap is a promising configuration, but its resistance is expected to far exceed the antenna resistance. Second, the antenna and diode must therefore be co-designed for conjugate matching, for example using nanocircuit loading concepts [32, 33], and the present port-based S_{11} should be re-evaluated with the diode impedance as the load. Third, a single bowtie is linearly polarised and captures at most half of unpolarised sunlight; crossed or dual-polarised bowties would remove this limitation. In addition, the partial spatial coherence of sunlight limits the power that a single small antenna can collect [8, 12]. From the numerical side, the present analysis considers an isolated element under port excitation. Future work will include (i) plane-wave receiving-mode simulations to quantify the field enhancement relative to incident sunlight, (ii) periodic-array simulations including mutual coupling and a possible back reflector, (iii) a finer frequency sweep and a mesh-convergence study above 850 THz, where higher-order modes appear, and (iv) fabrication by electron-beam lithography followed by optical characterisation and integration of an MIM diode.

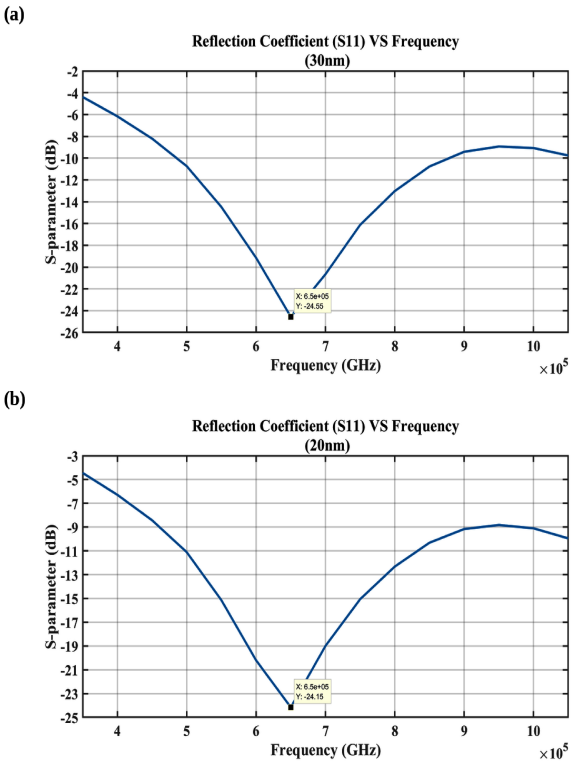


Fig. 7. Reflection coefficient (S_{11}) as a function of frequency for the silver bowtie nanoantenna with feed-gap widths of (a) 30 nm and (b) 20 nm.

© Ariston Publications 2026. All rights reserved.

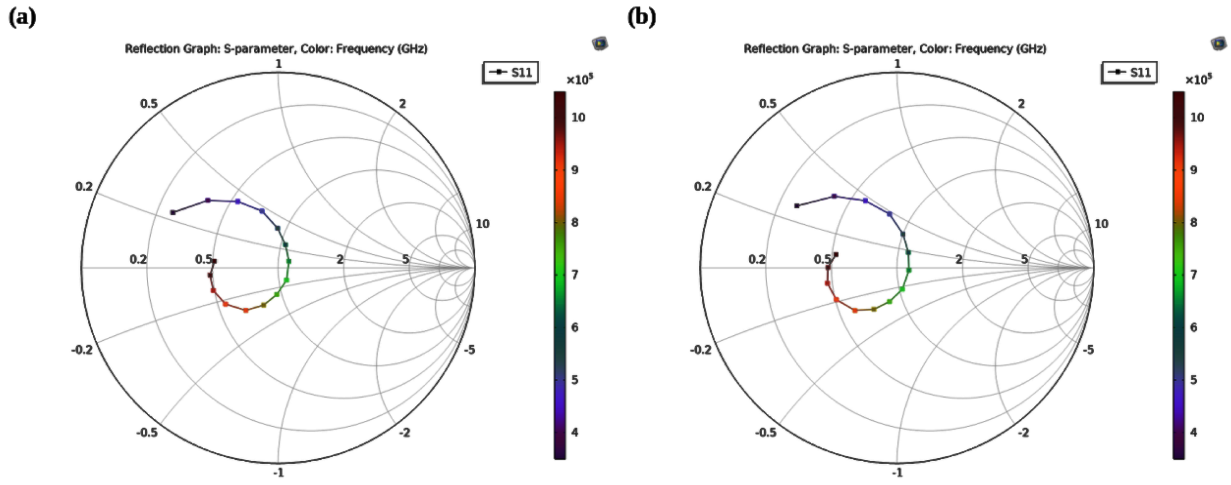


Fig. 8. Smith-chart representation of the reflection coefficient (S_{11}), normalized to the port reference impedance, for the silver bowtie nanoantenna with feed-gap widths of (a) 30 nm and (b) 20 nm. The colour scale indicates frequency in THz.

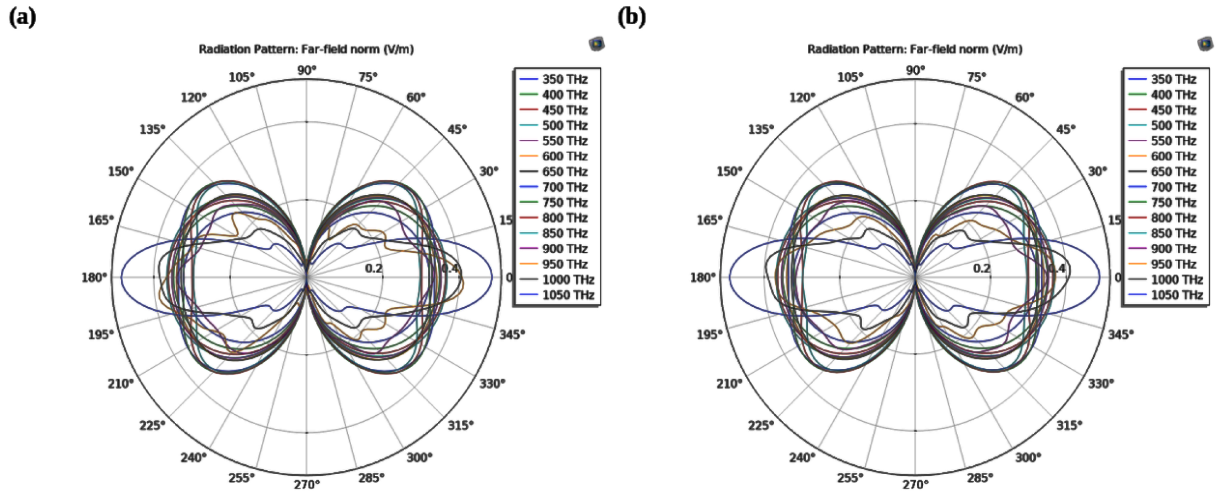
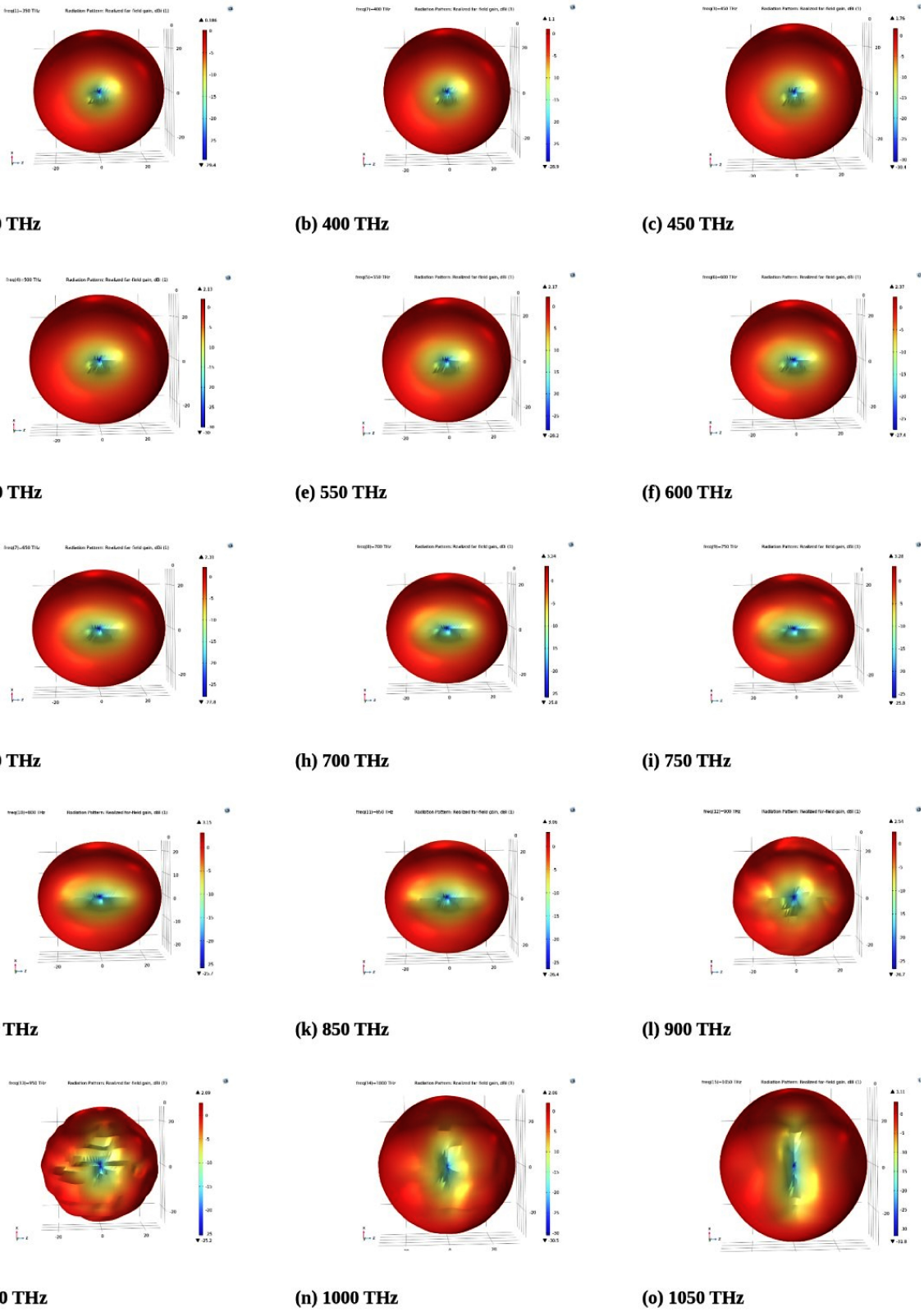


Fig. 9. Normalised two-dimensional far-field patterns (far-field norm) from 350 to 1050 THz for gap widths of (a) 30 nm and (b) 20 nm.

 © Ariston Publications 2026. All rights reserved.



(a) 350 THz **(b) 400 THz** **(c) 450 THz**

(d) 500 THz **(e) 550 THz** **(f) 600 THz**

(g) 650 THz **(h) 700 THz** **(i) 750 THz**

(j) 800 THz **(k) 850 THz** **(l) 900 THz**

(m) 950 THz **(n) 1000 THz** **(o) 1050 THz**

Fig. 10. Three-dimensional realised-gain patterns (dBi) for g = 30 nm from (a) 350 THz to (o) 1050 THz.

© Ariston Publications 2026. All rights reserved.

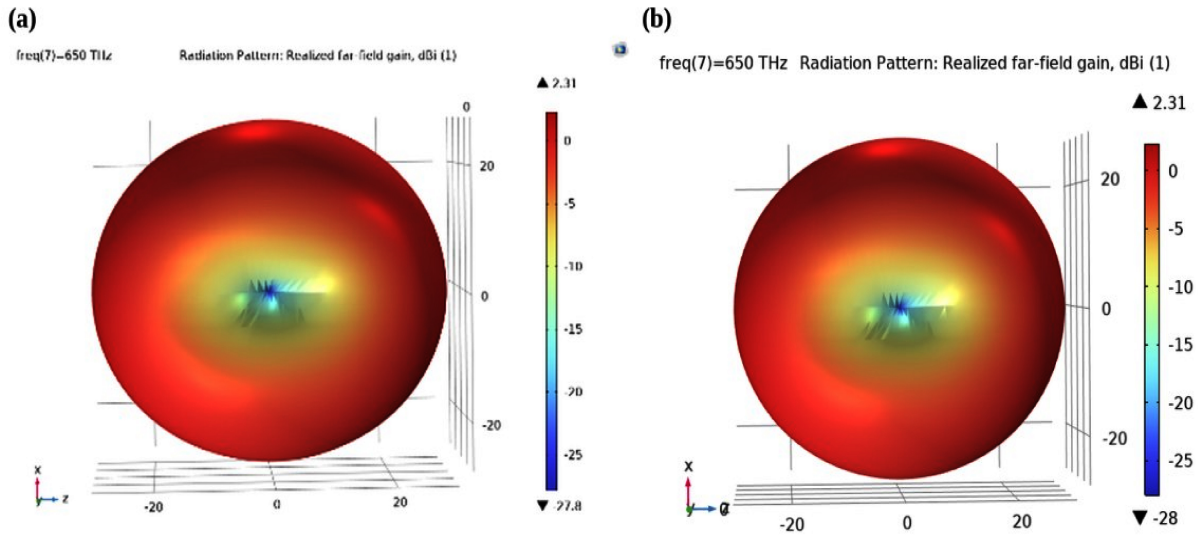


Fig. 11. Three-dimensional realised-gain pattern (dBi) at 650 THz for (a) g = 30 nm and (b) g = 20 nm.

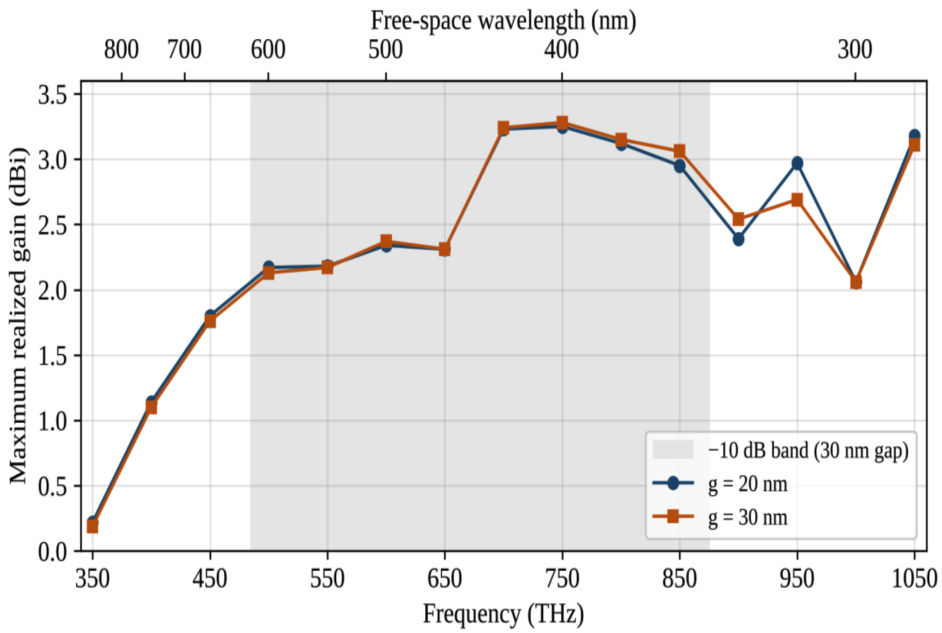


Fig. 12. Maximum realised gain versus frequency for the two gap widths. The shaded region marks the −10 dB impedance band of the 30 nm design; the top axis gives the free-space wavelength.

 © Ariston Publications 2026. All rights reserved.

4. CONCLUSION

A silver bowtie nanoantenna on a thin SiO_2 layer was designed for optical rectenna energy harvesting in the 350–1050 THz band and analysed by full-wave finite-element simulation for feed gaps of 20 and 30 nm. Both designs resonate at ≈650 THz with a minimum S_{11} of −24.2 dB (20 nm) and −24.6 dB (30 nm) and provide a −10 dB impedance bandwidth of ≈480–875 THz (≈57%). The maximum realised gain rises from ≈0.2 dBi at 350 THz to 3.25–3.28 dBi at 750 THz and remains between 2.1 and 3.3 dBi across the −10 dB band, with dipole-like radiation patterns up to ≈850 THz and higher-order-mode effects above. The strongest near fields occur in the feed gap, the natural location for a tunnelling diode; narrowing the gap from 30 to 20 nm raises the peak gap field by ≈50% while leaving the matching and gain essentially unchanged below 850 THz, which relaxes fabrication tolerances. These results establish the bowtie geometry as a robust, broadband receiving element for visible–near-infrared rectennas. Turning it into an efficient energy harvester will require codesign with an ultrafast rectifier, dual-polarised and array configurations, and experimental validation. With these steps, optical rectennas could complement photovoltaics as compact power sources for autonomous microsystems and sensor networks.

DECLARATIONS

Ethical Approval

We affirm that this manuscript is an original work, has not been previously published, and is not currently under consideration for publication in any other journal or conference proceedings. All authors have reviewed and approved the manuscript, and the order of authorship has been mutually agreed upon.

Funding

There are no funding

Availability of data and material

All of the data obtained or analyzed during this study is included in the report that was submitted.

Conflicts of Interest

The authors declare that they have no financial or personal interests that could have influenced the research and findings presented in this paper. The authors alone are responsible for the content and writing of this article.

Acknowledgments

The authors thank Madan Mohan Malaviya University of Technology, Gorakhpur, and the Nanofluid Laboratory of the Department of Physics and Material Science for providing computational facilities.

REFERENCES

[1] Lewis, N. S., **2016**. Research Opportunities to Advance Solar Energy Utilization. *Science*, 351, p.aad1920. https://doi.org/10.1126/science.aad1920.

[2] Haegel, N. M. Atwater, H. Barnes, T. others, **2019**. Terawatt-Scale Photovoltaics: Transform Global Energy. *Science*, 364, p.836-838. https://doi.org/10.1126/science.aaw1845.

[3] Shockley, W. Queisser, H. J., **1961**. Detailed Balance Limit of Efficiency of p-n Junction Solar Cells. *Journal of Applied Physics*, 32, p.510-519. https://doi.org/10.1063/1.1736034.

[4] Green, M. A. Dunlop, E. D. Levi, D. H. Hohl-Ebinger, J. Yoshita, M. Ho-Baillie, A. W. Y., **2019**. Solar Cell Efficiency Tables (Version 54). *Progress in Photovoltaics: Research Applications*, 27, p.565-575. https://doi.org/10.1002/pip.3171.

[5] Vullers, R. J. M. van Schaijk, R. Doms, I. Van Hoof, C. Mertens, R., **2009**. Micropower Energy Harvesting. *Solid-State Electronics*, 53, p.684-693. https://doi.org/10.1016/j.sse.2008.12.011.

[6] Bailey, R. L., **1972**. A Proposed New Concept for a Solar-Energy Converter. *Journal of Engineering for Power*, 94, p.73-77. https://doi.org/10.1115/1.3445660.

[7] Moddel, G. Grover, S., **2013**. Rectenna Solar Cells. *Rectenna Solar Cells*. https://doi.org/10.1007/978-1-4614-3716-1.

[8] Venbosch, G. A. E. Ma, Z., **2012**. Upper Bounds for the Solar Energy Harvesting Efficiency of Nano-Antennas. *Nano Energy*, 1, p.494-502. https://doi.org/10.1016/j.nanoen.2012.03.002.

© Ariston Publications 2026. All rights reserved.

[9] Grover, S. Moddel, G., **2011**. Applicability of Metal/Insulator/Metal (MIM) Diodes to Solar Rectennas. *IEEE Journal of Photovoltaics*, 1, p.78-83. https://doi.org/10.1109/JPHOTOV.2011.2160489.

[10] Sharma, A. Singh, V. Bougher, T. L. Cola, B. A., **2015**. A Carbon Nanotube Optical Rectenna. *Nature Nanotechnology*, 10, p.1027-1032. https://doi.org/10.1038/nnano.2015.220.

[11] Kotter, D. K. Novack, S. D. Slafer, W. D. Pinhero, P. J., **2010**. Theory Manufacturing Processes of Solar Nanoantenna Electromagnetic Collectors. *Journal of Solar Energy Engineering*, 132, p.011014. https://doi.org/10.1115/1.4000577.

[12] Corkish, R. Green, M. A. Puzzer, T., **2002**. Solar Energy Collection by Antennas. *Solar Energy*, 73, p.395-401. https://doi.org/10.1016/S0038-092X(03)00033-1.

[13] Joshi, S. Moddel, G., **2013**. Efficiency Limits of Rectenna Solar Cells: Theory of Broadb Photon-Assisted Tunneling. *Applied Physics Letters*, 102, p.083901. https://doi.org/10.1063/1.4793425.

[14] Novotny, L. van Hulst, N., **2011**. Antennas for Light. *Nature Photonics*, 5, p.83-90. https://doi.org/10.1038/nphoton.2010.237.

[15] Bharadwaj, P. Deutsch, B. Novotny, L., **2009**. Optical Antennas. *Advances in Optics Photonics*, 1, p.438-483. https://doi.org/10.1364/AOP.1.000438.

[16] Biagioni, P. Huang, J.-S. Hecht, B., **2012**. Nanoantennas for Visible Infrared Radiation. *Reports on Progress in Physics*, 75, p.024402. https://doi.org/10.1088/0034-4885/75/2/024402.

[17] Muhlschlegel, P. Eisler, H.-J. Martin, O. J. F. Hecht, B. Pohl, D. W., **2005**. Resonant Optical Antennas. *Science*, 308, p.1607-1609. https://doi.org/10.1126/science.1111886.

[18] Gadalla, M. N. Abdel-Rahman, M. Shamim, A., **2014**. Design, Optimization Fabrication of a 28.3 THz Nano-Rectenna for Infrared Detection Rectification. *Scientific Reports*, 4, p.4270. https://doi.org/10.1038/srep04270.

[19] Jayaswal, G. Belkadi, A. Meredov, A. Pelz, B. Moddel, G. Shamim, A., **2018**. Optical Rectification through an Al2O3 Based MIM Passive Rectenna at 28.3 THz. *Materials Today Energy*, 7, p.1-9. https://doi.org/10.1016/j.mtener.2017.11.002.

[20] Davids, P. S. Jarecki, R. L. Starbuck, A. others, **2015**. Infrared Rectification in a Nanoantenna-Coupled Metal-Oxide-Semiconductor Tunnel Diode. *Nature Nanotechnology*, 10, p.1033-1038. https://doi.org/10.1038/nnano.2015.216.

[21] Donchev, E. Pang, J. S. Gammon, P. M. others, **2014**. The Rectenna Device: From Theory to Practice (A Review). *MRS Energy Sustainability*, 1, p.E1. https://doi.org/10.1557/mre.2014.6.

[22] Briones, E. Alda, J. Gonzalez, F. J., **2013**. Conversion Efficiency of Broad-B Rectennas for Solar Energy Harvesting Applications. *Optics Express*, 21, p.A412-A418. https://doi.org/10.1364/OE.21.00A412.

[23] Tonouchi, M., **2007**. Cutting-Edge Terahertz Technology. *Nature Photonics*, 1, p.97-105. https://doi.org/10.1038/nphoton.2007.3.

[24] Siegel, P. H., **2002**. Terahertz Technology. *IEEE Transactions on Microwave Theory Techniques*, 50, p.910-928. https://doi.org/10.1109/22.989974.

[25] Byrnes, S. J. Blanchard, R. Capasso, F., **2014**. Harvesting Renewable Energy from Earth's Mid-Infrared Emissions. *Proceedings of the National Academy of Sciences*, 111, p.3927-3932. https://doi.org/10.1073/pnas.1402036111.

[26] Brown, G. H. Woodward, O. M., **1952**. Experimentally Determined Radiation Characteristics of Conical Triangular Antennas. *RCA Review*, 13, p.425-452.

[27] Balanis, C. A., **2016**. Antenna Theory: Analysis Design. *Antenna Theory: Analysis Design*.

[28] Fromm, D. P. Sundaramurthy, A. Schuck, P. J. Kino, G. Moerner, W. E., **2004**. Gap-Dependent Optical Coupling of Single Bowtie Nanoantennas Resonant in the Visible. *Nano Letters*, 4, p.957-961. https://doi.org/10.1021/nl049951r.

[29] Schuck, P. J. Fromm, D. P. Sundaramurthy, A. Kino, G. S. Moerner, W. E., **2005**. Improving the Mismatch between Light Nanoscale Objects with Gold Bowtie Nanoantennas. *Physical Review Letters*, 94, p.017402. https://doi.org/10.1103/PhysRevLett.94.017402.

 © Ariston Publications 2026. All rights reserved.

[30] Sundaramurthy, A. Crozier, K. B. Kino, G. S. Fromm, D. P. Schuck, P. J. Moerner, W. E., **2005**. Field Enhancement Gap-Dependent Resonance in a System of Two Opposing Tip-to-Tip Au Nanotriangles. *Physical Review B*, 72, p.165409. https://doi.org/10.1103/PhysRevB.72.165409.

[31] Kinkhabwala, A. Yu, Z. Fan, S. Avlasevich, Y. Mullen, K. Moerner, W. E., **2009**. Large Single-Molecule Fluorescence Enhancements Produced by a Bowtie Nanoantenna. *Nature Photonics*, 3, p.654-657. https://doi.org/10.1038/nphoton.2009.187.

[32] Alu, A. Engheta, N., **2008**. Input Impedance, Nanocircuit Loading, Radiation Tuning of Optical Nanoantennas. *Physical Review Letters*, 101, p.043901. https://doi.org/10.1103/PhysRevLett.101.043901.

[33] Huang, J.-S. Feichtner, T. Biagioni, P. Hecht, B., **2009**. Impedance Matching Emission Properties of Nanoantennas in an Optical Nanocircuit. *Nano Letters*, 9, p.1897-1902. https://doi.org/10.1021/nl803902t.

[34] Akyildiz, I. F. Jornet, J. M., **2010**. Electromagnetic Wireless Nanosensor Networks. *Nano Communication Networks*, 1, p.3-19. https://doi.org/10.1016/j.nancom.2010.04.001.

[35] West, P. R. Ishii, S. Naik, G. V. Emani, N. K. Shalaev, V. M. Boltasseva, A., **2010**. Searching for Better Plasmonic Materials. *Laser Photonics Reviews*, 4, p.795-808. https://doi.org/10.1002/lpor.200900055.

[36] Johnson, P. B. Christy, R. W., **1972**. Optical Constants of the Noble Metals. *Physical Review B*, 6, p.4370-4379. https://doi.org/10.1103/PhysRevB.6.4370.

[37] Malitson, I. H., **1965**. Interspecimen Comparison of the Refractive Index of Fused Silica. *Journal of the Optical Society of America*, 55, p.1205-1209. https://doi.org/10.1364/JOSA.55.001205.

[38] COMSOL AB, **2023**. COMSOL Multiphysics v. 6.2: RF Module User's Guide. *COMSOL Multiphysics RF Module User's Guide*.

[39] Berenger, J.-P., **1994**. A Perfectly Matched Layer for the Absorption of Electromagnetic Waves. *Journal of Computational Physics*, 114, p.185-200. https://doi.org/10.1006/jcph.1994.1159.

[40] Amestoy, P. R. Duff, I. S. L'Excellent, J.-Y. Koster, J., **2001**. A Fully Asynchronous Multifrontal Solver Using Distributed Dynamic Scheduling. *SIAM Journal on Matrix Analysis Applications*, 23, p.15-41. https://doi.org/10.1137/S0895479899358194.

[41] Pozar, D. M., **2012**. Microwave Engineering. *Microwave Engineering*.

ARISTON PUBLICATIONS

© Ariston Publications 2026. All rights reserved.